DOI: 10.13009/EUCASS2023-468
Aerospace Europe Conference 2023 – 10TH EUCASS – 9TH CEAS

Interaction between a moving droplet and an acoustic wave - 10^{th} EUCASS - 9^{th} CEAS

Ronan PLIQUE[⋆†♯], *Philippe GRENARD*[⋆], *Julien LABAUNE*[⋆], *Joël DUPAYS*[⋆]
[⋆]*DMPE, Onera, université Paris Saclay, F-91123 Palaiseau - France*
[♯] Cnes - transport spatial - établissement de Daumesnil, F-75612, Paris Cedex, France
Address
ronan.plique@onera.fr
[†]Corresponding author

Résumé

An overlapping mesh method is used to study the momentum interactions between a rigid spherical particle and the surrounding viscous flow. The calculation methodology is developed and validated in the case of a stationary flow, first in the Stokes regime and then for higher Reynolds numbers, by comparing the calculated drag force with the available analytical and empirical results. The approach is then applied to the case of a particle undergoing a low-amplitude oscillating motion in a fluid at rest to consolidate the approach in the unsteady regime. Here again, the comparison between simulation and theory is satisfactory and allows us to look forward with confidence further study in the non-linear acoustic regime.

1. Introduction

In space propulsion, the interaction between a spray and an acoustic wave can be found in the combustion chambers of liquid rocket engines (LRE[3]) and in solid rocket engines (SRE[8]). In LRE, the interactions are linked to a coupling between the atomization process, the combustion, and the acoustics of the chamber. The most feared resonance modes are the transverse modes which are at high frequencies due to the size of the engine. They can cause an increase of the average chamber pressure and of the heat fluxes on the wall. In SRE, in order to improve the engine capabilities, aluminum particles are usually introduced into the propellant. These particles can create instabilities by interacting with the combustion process, the flow field, and the acoustics of the chambers which can cause severe damage to the engine and to the rocket.[11] Interactions of spray with acoustics fields also occur on a large scale during the deluge of water at lift-off (figure 1a). The purpose of the deluge is to reduce the heat flux undergone by the launch pad to protect its integrity (figure 1b) and to attenuate the acoustic environment to protect the payload, the structure, and onboard equipment of the launcher, as well as the ground support equipment. This study focuses only on this last issue.

Noise reduction is achieved by optimizing the design of the deflectors, providing soundproofing solutions for the launcher fairing, and relying on water deluge. This latter technique could reduce noise by as much as $8-12$ dB (Kandula[14]) compared to a total acoustic power of 180 dB delivered for instance during the launch of the European rocket Vega.[22] Water injection mitigates noise mainly by reducing jet exhaust speed and temperature. An acoustic wave is an alternation between a pressure zone and a depression zone. This pressure gradient leads to a velocity field in gases, and the inertia of the droplets leads to a velocity difference between gas and droplets. This difference allows the transfer of momentum from the flow to the droplets. In this way, the acoustic wave loses acoustic intensity as it passes through a droplet mist. As for temperature reduction, this is achieved by a high heat capacity and a significant enthalpy of vaporization of the droplets.

At Onera, the issue of the acoustic environment at the lift-off has been tackled for a long time. The most recent work includes those by Langenais[16] and by Dargaux,[9] who have developed a numerical methodology for calculating the acoustics field produced by the jet regardless of the droplet mist. Of course, the long-term objective is to build a validated methodology that considers the effect of the deluge. However, introducing this effect into the numerical methodology first requires the development of suitable gas-droplet interaction models. The aim of this work is to contribute to the development of such models.

Due to the complexity of the flows and the multiple interactions, it is tempting to use numerical simulations to guide launch pad design and optimize the water-to-jet mass flow rate ratio, injection process, and characteristics (choice,

DOI: 10.13009/EUCASS2023-468

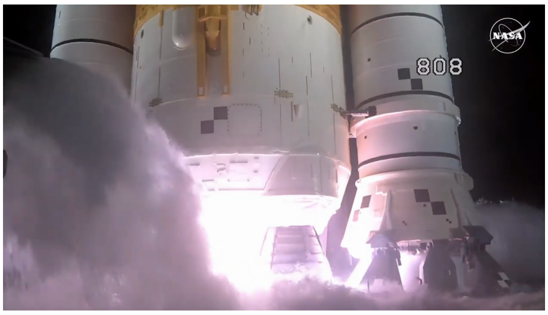

(a) Water deluge during Artemis 1 lift-off

(b) Launch-pad after Starship-Super Heavy lift-off

FIGURE 1 – Importance of the deluge for the launch-pad

number and position of injectors, spray velocity and temperature, ...). To simulate the behavior of the spray and cross-interaction with the acoustic field we can use a Lagrangian or Eulerian approach in dilute assumption assuming low occupancy volume of the dispersed phase. In these models, the mass, momentum, and energy exchange terms relate to an isolated droplet and assume steady or quasi-steady exchange models between the droplet and the surrounding gas.

In other words, the sound field must be low-level and respect the conditions of linear acoustics, which is not the case for a pressure variation corresponding to 180 dB, i.e. 0.2 bar or 20%. This pressure variation is too large for steady and quasi-steady models to be relevant for all frequencies and droplet diameters. So we need to go back to the scale of a single droplet to reformulate the models on a more global scale. There are many methods that can simulate the interaction between a flow and a few inclusions like droplets, bubbles, or particles. In many methods, the calculation is performed from the inclusion point of view and the disturbance/flow is imposed upstream. Such approaches do not allow to consider the back effect of the droplet motion on the flow. To manage two-way interaction correctly, it is necessary to work in the laboratory frame of reference as enabled by some approaches like VOF, Level Set (Tryggvason[25]), Diffuse Interface (Kapila[15]), Immersed Boundary (Tenneti[24] and Chadil[6]), or body-fitted (Maury[17] and Hu[13]) methods. The approach used in this work belongs to the last category and will be used, as a first step, to address only the momentum exchange term in case of a rigid, isothermal, and inert surface.

The paper is organized as follows. In section 2, we first introduce the theoretical developments that will be used to validate the method and establish a suitable calculation methodology. Section 3 is devoted to the presentation of the method, and section 4 and 5 present its validation under steady-state and oscillating conditions respectively. An assessment of the efficiency and potential of the approach is presented in conclusion, together with an outlook on future work.

2. Analytical development

Steady state To begin with, we will seek to determine the value of the force acting on a sphere under a steady motion. Those analytical developments were first carried out by Stokes,[23] who was interested in the motion of a clock pendulum and the resistance of air to that motion. In his calculation, Stokes, neglect the influence of the string and he considered his pendulum to be a particle with motion. With the reference frame $(O, \vec{i}, \vec{j}, \vec{k})$ at the center of the particle, the flow around it is governed by the following Navier-Stokes equations :

$$\rho_f \left(\frac{\partial \vec{v_f}}{\partial t} + \left(\vec{v_f} . \overrightarrow{grad} \right) \vec{v_f} \right) = -\overrightarrow{grad}\left(P_f\right) + \mu_f \Delta \left(\vec{v_f}\right) + \rho_f \vec{g} + \frac{\mu_f}{3} \overrightarrow{grad}\left(div \left(\vec{v_f} \right) \right) \quad (1)$$

With ρ_f the density of the fluid, P_f the pressure, $\vec{v_f}$ the velocity field, $\vec{g}$ the gravitational force field by mass unit and μ_f his viscosity. The Stokes regime is characterised by a predominance of viscous terms over inertial terms. If the fluid is incompressible and the external forces are negligible like the inertial term, the equation (1) can be put in the following form :

$$\overrightarrow{grad}\left(P_f\right) = \mu_f \Delta \left(\vec{v_f}\right) \quad (2)$$

As some of the boundary conditions are defined on the surface of the particle of radius R_p, it is easier to solve equations in spherical coordinate $(\vec{e}_r, \vec{e}_\theta, \vec{e}_\psi)$. By choosing to orientate the z axis in the direction of flow, the motion is rotationally symmetrical about this axis and the velocity field depends only of r and θ. So it is possible to define ψ such that, for $r > R_p$:

DOI: 10.13009/EUCASS2023-468

$$\vec{v_f} = \frac{1}{r^2 sin(\theta)} \left(\overrightarrow{grad}(\psi) \wedge \vec{e}_\phi\right) \tag{3}$$

This leads to :

$$\vec{\Omega} = \overrightarrow{rot}\left(\vec{v_f}\right) = \frac{-E^2\psi}{r sin(\theta)}.\vec{e}_\phi \ ; \ E^2 = \frac{\partial^2}{\partial r^2} - \frac{cos(\theta)}{r^2 sin(\theta)}\frac{\partial}{\partial\theta} + \frac{1}{r^2}\frac{\partial^2}{\partial\theta^2} \tag{4}$$

Equation (2) is rewritten as the following system :

$$\frac{\partial P_f}{\partial r} = \frac{\mu_f}{r^2 sin(\theta)}\frac{\partial\left(E^2\psi\right)}{\partial\theta} \tag{5}$$

$$\frac{\partial P_f}{\partial\theta} = -\frac{\mu_f}{sin(\theta)}\frac{\partial\left(E^2\psi\right)}{\partial r} \tag{6}$$

Next, we will subtract the cross-differentiation of (5) with respect to θ $\left(\frac{\partial}{\partial\theta}\right)$ with the cross-differentiation of (6) with respect to r $\left(\frac{\partial}{\partial r}\right)$ to obtain :

$$E^2\left(E^2\psi\right) = 0 \tag{7}$$

We can then deduce, with the no slip-condition at $r = R_p$ and a uniform upward velocity field ($\vec{v_f} = U_\infty\vec{k}$) away from the droplet ($r = \infty$) that :

$$\psi(r,\theta) = \frac{-U_\infty}{4}\left(-3R_p r + \frac{R_p^3}{r} + 2r^2\right) sin^2(\theta) \tag{8}$$

The first term is called the Stokeslet (viscous correction), the second one is the doublet (another correction term), and the last one corresponds to the viscosity far away from the sphere. From that results, we can deduce the velocity field :

$$\vec{v_f} = \frac{-U_\infty cos(\theta)}{2}\left(\frac{-3R_p}{r} + \frac{R_p^3}{r^3} + 2\right)\vec{e}_r - \frac{-U_\infty sin(\theta)}{4}\left(\frac{3R_p}{r} + \frac{R_p^3}{r^3} - 4\right)\vec{e}_\theta \tag{9}$$

The equations (5) and (6) lead to :

$$P_f(r,\theta) = \frac{3}{2}\frac{R_p}{r^2}U_\infty\mu_f cos(\theta) \tag{10}$$

Finally what is left is to get the surface force by using the shear stress formula, knowing that the flow is symmetrical with respect to θ and ϕ. So we need τ_{rr} and $\tau_{r\theta}$ which can be written in the following forms :

$$\tau_{rr} = 2\mu_f\frac{\partial v_{f_r}}{\partial r} \tag{11}$$

$$\tau_{r\theta} = \mu_f\left[r\frac{\partial}{\partial r}\left(\frac{v_{f_\theta}}{r}\right) + \frac{1}{r}\frac{\partial v_{f_r}}{\partial\theta}\right] \tag{12}$$

The result obtain is parallel to the z axis :

$$\vec{F_D} = \int\int\left(\left(-P_f(r,\theta) + \tau_{rr}\right).\vec{e}_r + \tau_{r\theta}.\vec{e}_\theta\right)dA = 6\pi\mu_f R_p U_\infty\vec{k} \tag{13}$$

From this expression, Stokes defined the drag coefficient C_D which is the ratio of the drag force ($\vec{F}_D$) and the cross-sectional area ($A = \pi R_p^2$) times the far field dynamic pressure ($\frac{1}{2}\rho_f U_\infty^2$) :

$$C_D = \frac{F_D}{\frac{1}{2}\rho_f A U_\infty^2} \tag{14}$$

Which can be expressed as a function of the Reynolds number :

$$C_D = \frac{24}{Re} \qquad \text{with } Re = \frac{\rho_f D_p U_\infty}{\mu_f} \ ; \ D_p = 2R_p \tag{15}$$

DOI: 10.13009/EUCASS2023-468

This equation is only available for $0 < Re < 2$. Precise correlations for a wide range of Reynolds variations are given in Clift et al[7] (table 5.2). In section 4, we will use them to validate the numerical method both in the Stokes and laminar regimes.

Unsteady state Later Boussinesq,[4] Basset,[2] and Oseen[20] independently extended this work to the case of a sphere in rectilinear motion in an incompressible viscous fluid at rest, obtaining the so-called **Boussinesq-Basset-Ossen** (BBO) equation. But it was not until 1983, with the work of Maxey and Riley[18] and that of Gatignol,[12] that a rigorous expression was established for the motion of a rigid, non-rotating sphere moving in an unsteady, spatially inhomogeneous flow at low Reynolds number. Under these hypotheses, the total force applied to the particle can be separated into different contributions :

$$\sum \vec{F}_{ext} = \vec{F}_g + \vec{F}_D + \vec{F}_H + \vec{F}_{Ma} + \vec{F}_{Tchen} \tag{16}$$

The first one $\vec{F}_g$ represents the buoyancy. It regroups the forces linked to gravity such as weight and Archimedes's principle, and can be expressed as follows :

$$\vec{F}_g = \rho_p (1 - \Phi) \frac{\pi D_p^3}{6} \vec{g} \tag{17}$$

With $\Phi = \dfrac{\rho_f}{\rho_p}$ the density ratio and ρ_p the density of the particle. However, as the particle is much denser than the air, the Φ contributions can be neglected.

The second term $\vec{F}_D$ is the steady drag force. This force can be seen as the sum of all effects that oppose the relative motion of the particle with respect to the flow. This force can be expressed as :

$$\vec{F}_D = 3\pi\mu_f D \left(\vec{v_f} - \vec{V_p}\right) \tag{18}$$

With $\vec{V_p}$ the particle velocity.

The third term $\vec{F}_H$ is the Basset-Boussinesq force. In an initially uniform viscous fluid, a change in the velocity of the fluid, such as an oscillating particle, will take some time to diffuse to the whole medium. The reaction force exerted on the droplet is therefore not the same as that which would be exerted for a uniform flow. There is a certain delay which is greater with higher viscosity. Because of this delay, the force on the droplet during the first oscillation is different from that during the next one. The Basset-Boussinesq force reflects the memory of the relative accelerations between the particle and the fluid and is expressed as :

$$\vec{F}_H = \frac{3}{2} D_p^2 \sqrt{\pi \rho_f \mu_f} \int \frac{d}{d\tau} \left(\vec{v_f} - \vec{V_p}\right) \frac{d\tau}{\sqrt{t - \tau}} \tag{19}$$

Where $\frac{d}{dt}$ is the material derivative following the center of the particle.

The fourth term, $\vec{F}_{Ma}$ represents the added mass force. This force is due to the mass of the fluid that the particle needs to put in motion in order to move. With the minor but rigorous correction proposed by Auton et al.,[1] this term is written as :

$$\vec{F}_{Ma} = \rho_f \frac{\pi D_p^3}{12} \left(\left. \frac{D\vec{v_f}}{Dt} \right|_{x_p} - \frac{d\vec{V_p}}{dt} \right) \tag{20}$$

Where $\frac{D}{Dt}$ is the material derivative following the fluid element. To simplify the expression of these three forces, we have deliberately assumed a spatially homogeneous flow. In the general case, it appears additional terms known as Faxen's corrections, functions of the Laplacian of the fluid velocity field.

The fifth term, $\vec{F}_{Tchen}$, represents the force that the same volume of fluid would experience in the absence of the particle. Its expression is as follows :

$$\vec{F}_{Tchen} = \rho_f \frac{\pi D_p^3}{6} \left. \frac{\partial \vec{v_f}}{\partial t} \right|_{x_p} \tag{21}$$

Parmar[21] has also adopted this approach in order to propose an equation of motion valid for compressible flow. Outside the Stokes regime, there are no analytical solutions, and numerous empirical models deduces from experimental data or simulations, have been proposed in the literature. Many of them, such as the Odar and Hamilton[19] model assumes that the various contributions remain independent and that the effect of the Reynolds number can be simply

DOI: 10.13009/EUCASS2023-468

rendered by multiplying each of the terms by a coefficient depending on this Reynolds number. For instance, the drag force becomes :

$$\vec{F}_D = \rho_f \frac{\pi D_p^2}{C_D} \left\|\vec{v_f} - \vec{V_p}\right\| \left(\vec{v_f} - \vec{V_p}\right) \tag{22}$$

In the Stokes regime, velocity shear does not produce a resultant force but for higher relative velocities, it may be necessary to add the contribution of side forces like the lift force and the Magnus effect.

Oscillatory motion In the special case of a rigid non-rotating particle performing small translational oscillations in a fluid at rest, it can be shown[10] that the forces applied to it are in the following form :

$$\vec{F} = 6\pi\mu_f R_P \vec{V_p} + 6\pi\mu_f \frac{R_P^2}{\delta} \vec{V_p} + 3\pi R_P^2 \rho_f \delta \frac{d\vec{V_p}}{dt} + \frac{2\pi R_P^3}{3} \rho_f \frac{d\vec{V_p}}{dt} \tag{23}$$

With $\delta = \sqrt{\frac{2\nu_f}{\omega}}$ the penetration depth. This quantity, where $\nu_f = \frac{\mu_f}{\rho_f}$ is the fluid kinematic viscosity, corresponds to the thickness of the acoustics boundary layer. If the velocity of the droplet is of the form $\vec{V_p} = U_0 cos(\omega t)\vec{k}$ at low frequencies the force on the droplet can be reduced to the equation (13).

To obtain this expression, the convection terms have been neglected and, for this approximation to hold true, the Reynolds number must be small compared to 1, or the amplitude of the motion of the droplet must be small compared to its radius. The first term of the equation (23) represents the Stokes drag, and the last term represents the added mass forces. Terms 2 and 3 represent the Basset-Boussinesq force.

Comparison of the two formulations In figure 2, the evolution of the various force expressed in equation (16) and (23) have been plotted. The steady drag ($6\pi\mu_f R_p \vec{V_p}$), is expressed in the same way in both equation and its plot for reference. Even if the expression of the added mass forces is expressed in a variety of ways, the corresponding curves are superimposed (green and orange lines). The difference between these expressions is to seek in the Basset-Bousinesq force. The two expressions have been determined with a particle oscillating in a fluid at rest at low Reynolds.

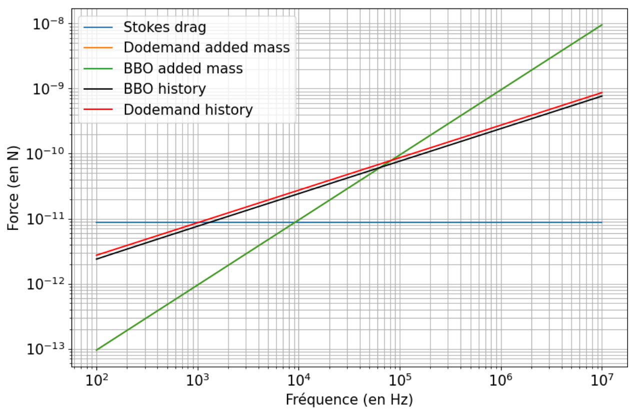

FIGURE 2 – Comparison between the formulations from the BBO equation and the Dodemand equation[10] (eq23)

Due to the fact that the two models defined by equations (16) and (23) behave in the same way when the frequency of calculation evolves and that the difference between the two is extremely small, we will use the model defined by Dodemand, equation (23), which is simpler than that of BBO, equation (16), in order to characterise the performance of our numerical method.

3. Numerical method

Now that some analytical results have been presented and found a comparison point between the theoretical and numerical results, we are going to list the various ways to simulate the interaction between an inclusion and the surrounding gas.

The first approach called *body fitted* aims to explicitly mesh the boundary of the inclusions, which allows the fluid-structure interactions to be calculated rigorously but requires a regular remeshing of the domain according to the

DOI: 10.13009/EUCASS2023-468

position of inclusions. However, with a rigorous calculation at the interface, we can accurately obtain the stress torsor and the set of fluid-structure interactions for any flow. This method doesn't allow the deformation of inclusions and requires more computing time due to the remeshing and the interpolation of the characteristic quantities of the flow on the new mesh.

The second approach called *immersed boundary method*, adds to the Navier-Stokes equations a forcing term applied to the exact position of the boundary. The goal of this term is to reproduce the effect of the inclusion's boundary in relative motion with respect to the fluid. This approach is used in the aeroelasticity domain for immersed body and allows the use of greatly simplified meshes than in the *body fitted* method and bodies are not explicitly discretised. The two first approaches are used with solid inclusion or with the hypothesis of indeformability.

With the two last approaches, it is possible to simulate large deformations of fluid inclusions. By the use of methods with lagrangian tracking or eulerian description (*Volume Of Fluid*, *level-set* or a hybrid method compensating for the shortcomings of both methods) that follow and reconstruct the interface into each cell for the third one.

At last, by allowing the interface to spread over several mesh cells due to the effect of numerical diffusion, the last one is called *diffuse interface*. This method eliminates the need for tracking and reconstruction of the interface. A homogenisation process is used to obtain averaged equations with interfacial transfer terms that must be modelled.

This paper seeks to determine momentum exchange in a two-way coupling strategy between a droplet and an unsteady flow field. To do that, a body-fitted approach will be used, based on the idea of Brenner,[5] who has developed an overlapping method to make it easier to simulate flows over complex structures with relative motion with each other in a hex-dominant framework. The method developed in Onera's in-house CFD code Cedre is based on these ideas, for generalized polyhedral meshes, in a parallel environment and implicit numerical schemes and is called *Maillage Chevauchant Conservatifs* (MCC). It is based on two meshes, one for the background, which is intersected by the inclusion's mesh. Inter-mesh communication is thus computed from the exact geometry intersections. It is different from classical chimera overlapping methods in the fact that it doesn't need an interpolation step (in general no conservative) between the two meshes.

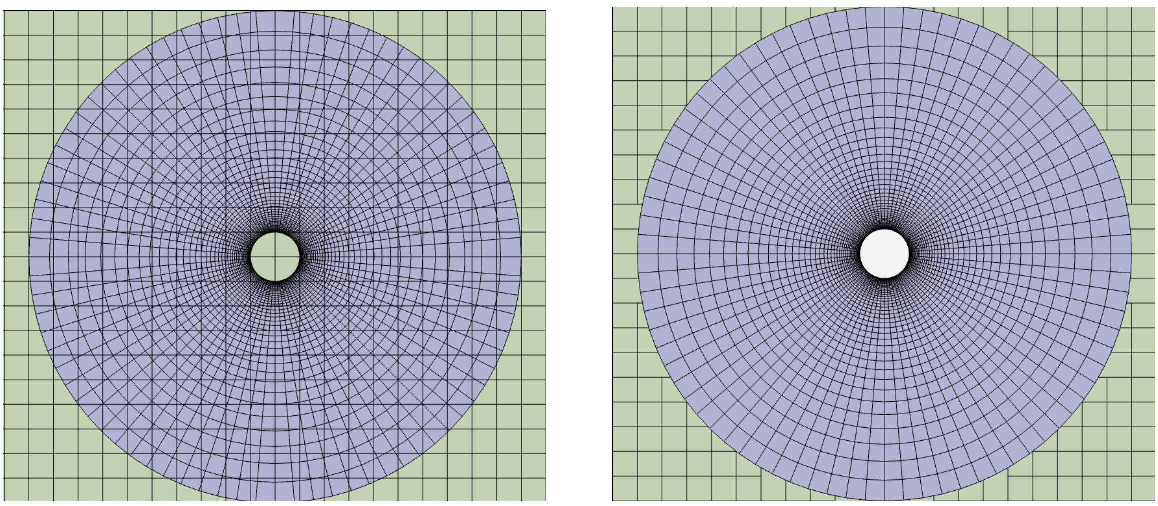

(a) Original meshes

(b) Mesh after the MCC

Figure 3 – Illustration of the MCC on a 2D mesh

Figure 3b shows the result of the application of the MCC on a 2D mesh. The green one is the background mesh and will serve as the reference frame, the purple one is the inclusion mesh. The advantage of this method is that the inclusion mesh can move during the computation with the application on the surface of the fluid force. Moreover, we save the two meshes and their scalars and vectors field at the end of each iteration, which allows us to skip a costly interpolation step and stay conservative. It allows us to calculate the stress torsor on an unalterable droplet and, with the first law of Newton, to deduce its new speed and position by numerical integration. Generally, we can have all the exchange of momentum, mass, and energy between the droplet and the fluid while taking into account the unsteady effects induced by the feedback of the medium disturbed by its motion while remaining in an inertial reference frame.

DOI: 10.13009/EUCASS2023-468

4. Verification of the method under steady-state conditions

4.1 Data set

To simulate the interaction between a steady flow and an inclusion we will consider a volume of control around it. The background mesh (fig 4c) will be a cylinder with input-output conditions at the base level and the no-slip condition on the wall. For the inclusion mesh, we have some layers of prisms around the inclusion (fig 4b). The inside of the inclusion will not be meshed and its boundary will be considered as an adiabatic wall. The general geometry of the simulation is a volume of control with a radius of 7 mm, a height of 20 mm around a droplet with $R_p = 0.5\ mm$.

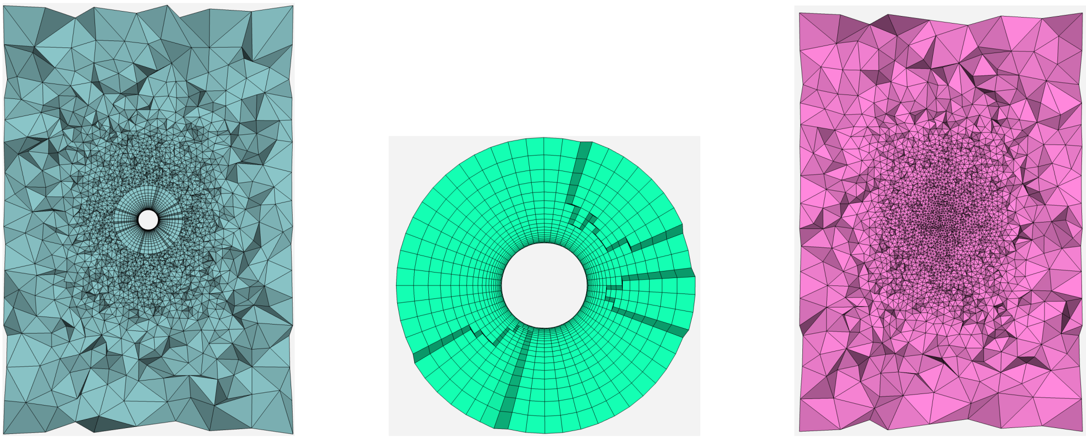

(a) Static mesh (b) Mesh around the droplet (c) Background mesh

FIGURE 4 – Mesh used for the calculation

The first mesh that will be used in the simulation, will be the mesh shown in figure 4a. This case allows us to determine the differences between the correlation of Clift[7] and our simulations. It doesn't use the MCC algorithm and will be referenced as *Staticmesh*.

As said previously, the inclusion mesh can move during the calculation by integration of the forces all around the inclusion surface. But in order to move the mesh with the right amplitude, we need to give it a mass. So, we will have two different cases when we use the MCC, in the first one the inclusion mesh will have a mass corresponding to the one of a water droplet with a diameter of 1 millimeter ($5,22.10^{-7}$kg). This case will be referenced as *MCC-moving* in the rest of the paper. In the second case, the MCC algorithm allows us to make the inclusion motionless in order to have the magnitude of the error due to the MCC intersection process. We will refer to this case as *MCC-fixed*. The difference between *MCC-fixed* and *MCC-moving* will be due to the displacement of the inclusion mesh (figure 4b). Whereas the difference between *MCC-moving* and *Staticmesh* is linked to the approximations made by the algorithm during the intersection.

Numerical solving technique We will use a second-order spatial discretization and some low-Mach correction in our compressible code. The time integration is done with a first-order implicit Euler scheme. The fluid used is air with a possible change in viscosity in order to change the Reynolds number without changing the velocity flow. The bottom surface, at $z = -10mm$, is the area where the air is injected into the simulation at the speed U_{int} and the top surface, at $z = 10mm$, represent the outlet of the simulation at pressure P_{out}.

4.2 Results

4.2.1 Study on the *Staticmesh* case

With a Reynolds number below 2, the drag coefficient can be seen as only a function of the Reynolds number with the equation (15). However, the Reynolds number depends on 4 physical variables. It is important to check if, the coefficient drag obtain by our numerical method has the same behavior whether the speed or viscosity changes for the same Reynolds number. In order to have a Reynolds number lower than 2 with air, the velocity of the fluid at the injection level need to be lower than $3,20.10^{-2} m.s^{-1}$. At this speed, we are expecting to have a force acting on the

DOI: 10.13009/EUCASS2023-468

droplet with a magnitude of $5,6.10^{-9}N$. To have a better quantification of the numerical error of our method, and to prevent the flow to be at a very low Mach number, we have decided to use a higher viscosity ($\mu_f = 1,856.10^{-2}Pa.s$) and injection speed ($U_{int} = 30m.s^{-1}$) to obtain a Reynolds of $Re = 1,88$. With these values, the expected force is about $5,25.10^{-3}N$ To decrease the Reynolds number we will change either the viscosity or the velocity of the simulation. And in order to calculate the drag coefficient of each simulation we will measure the actual velocity as well as the effective density and viscosity upstream of the droplet. The drag force acting on the droplet will be measured too and the drag coefficient will be calculated with the equation (14) with $U_\infty = \left\|\vec{v_f} - \vec{V_p}\right\|$.

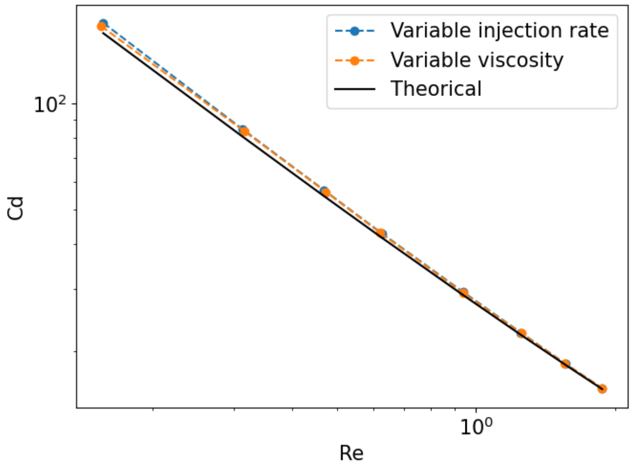

FIGURE 5 – Drag coefficient as a function of Reynolds for a variable viscosity or speed

In figure 5, we can see that the drag coefficient is nearly the same when the viscosity change or when the injection velocity change for the same Re. At very low Reynolds, the numerical results at variable speed are further away from the experimental curve than those obtained by controlling the viscosity. In fact, as the CFD code used is a compressible one, it loses accuracy when the Mach number becomes too low.

4.2.2 Comparison between *Staticmesh*, *MCC-fixed*, and *MCC-moving*

To keep this numerical error away, we will use only the results obtained by changing the viscosity of the fluid for the rest of the study. The error between the *Static mesh* and Clift's[7] correlations are of the order of 3%. The same computation are carried out with *MCC-moving* and *MCC-fixed*, and results are presented in figure 6a

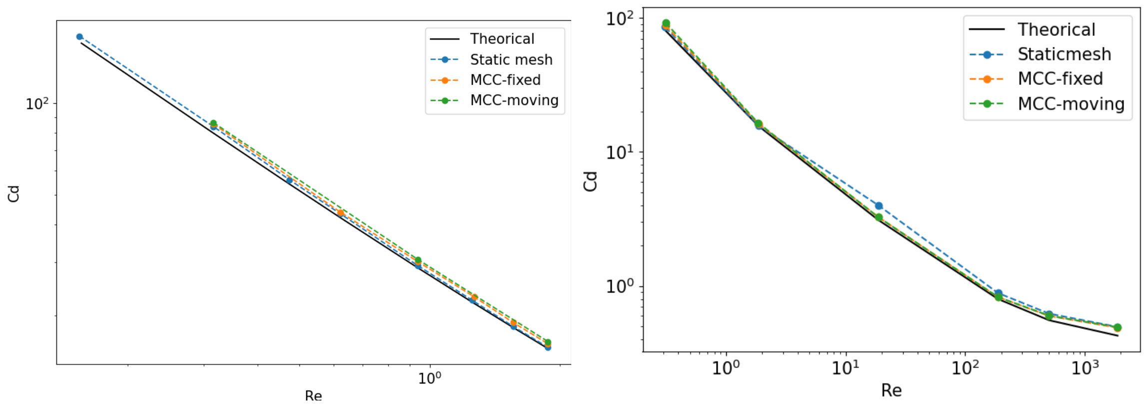

(a) Stokes' regime (b) Laminar flow

FIGURE 6 – Drag coefficient for *Staticmesh*, *MCC-fixed* and *MCC-moving*

In this figure 6a, we can see that the drag coefficient obtained in the *MCC-moving* case is slightly higher than those obtained with the *MCC-fixed* case. As the droplet also moves, the post-treatment based on the velocity difference between the droplet and the surrounding fluid is a bit more tricky and can explain these small differences.

DOI: 10.13009/EUCASS2023-468

4.2.3 Extension to laminar flow

The Reynolds number of interest is a particle-based Reynolds number, which depends on the velocity difference between the particle and the surrounding flow. For small particles, we can expect to stay in the laminar regime. If we increase the Reynolds number of our simulation we obtain the figure 6b. To do those simulations we have reduced the viscosity to the original air viscosity ($1,856.10^{-5}Pa.s$) while maintaining the injection velocity at $30m.s^{-1}$. As we can see, the results obtained with the simulation follow the variation of the theoretical curve. Overall the difference between the results from *MCC-moving* and the correlation curve do not exceed 5%. So with these differences between the two cases, we can assume that our method is precise enough to use it under unsteady conditions.

4.2.4 Streamlines

The method used gives accurate integral forces on the sphere. Moreover, if we look at the flow around the droplet, e.g. at a Reynolds number of 188, we can compare the separation point given by the computation to an experimental correlation. In the figure 7a we can see the recirculation area downstream of the droplet. From those streamline we can calculate the location boundary layer separation point. This point forms an angle of $118 \pm 2°$ with the front stagnation point and the center of the droplet. The uncertainty range of $2°$ is linked to the azimuthal discretization of the droplet. With a characteristic mesh size of $\Delta_{mesh} = 1,15.10^{-5}m$, it is possible to calculate an equivalent angle by dividing the azimuthal discretization by the droplet's radius. If we proceed this way, we find an uncertainty angle of $\Delta\theta = \frac{\Delta_{mesh}}{R} = 1,32°$, by rounding up we obtain the uncertainty range of $2°$. According to Clift[7] for a flow with a Reynolds number between 20 and 400, the localisation of the boundary layer separation point checks the following formula :

$$\theta_s = 180 - 42,5\left(ln\left(\frac{Re}{20}\right)\right)^{0,483} \tag{24}$$

In our condition we obtain that theoretically, the boundary layer separation point is at $\theta_s = 117,25°$. So the theoretical value is on the uncertainty range of the simulation done with the *Staticmesh* case.

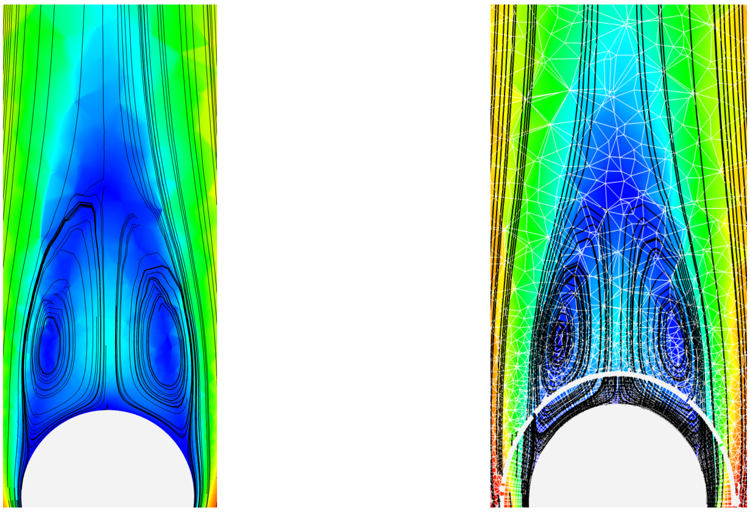

(a) Staticmesh

(b) *MCC-moving*

FIGURE 7 – Streamline at Re=188

Figure 7b shows the same streamlines for the *MCC-moving* case. The white circle around the sphere is located at the intersection between overlapping meshes. the separation point for *MCC-moving* is at an angle of $117 \pm 2°$ with respect to the front stagnation point. The theoretical angle of the separation point is within the uncertainty range of our two simulations.

4.3 Summary of results and conclusion

We have seen that the numerical method chosen to capture, with low uncertainties the amplitude of the force that is applied on the droplet in the case of a steady flow with a low Reynolds number. When the Reynolds number

DOI: 10.13009/EUCASS2023-468

increases, the drag coefficient is calculated to follows the same variation as the theoretical drag coefficient correlated by Clift. The drag applied to the droplet can be separated into two components. The evolution of those components follows the formula in the Stokes regime. Outside the Stokes regime, the diminution of the viscous drag can be explained by the position of the separation point. The evolution of the form drag can be explained by the pressure variation between the upstream and downstream of the droplet.

5. Use of the method under non-steady-state conditions

5.1 Data set

Now that we have determined the performance of the MCC in steady-state conditions, we will use this method in unsteady conditions. The analytical development that led us to the equation (23) has been done with a moving droplet in a fluid at rest. We will do the same using the geometry presented in figure 8a. The external boundary layer, at $R_p = 1mm$, is considered as a Dirichlet boundary at $1bar$, $300K$ and $0m.s^{-1}$. The surface of the droplet, at $R = 50\mu m$, will be considered an adiabatic wall. The position of the center of the droplet is prescribed to a sinusoidal evolution : $X_{drop} = \frac{U_0}{\omega} sin(\omega t)$. The droplet mesh shown in figure 8b has been unrefined for a better view of the mesh topology around the droplet.

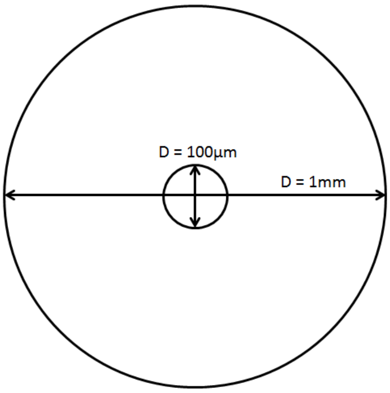

(a) Sketch of the geometry

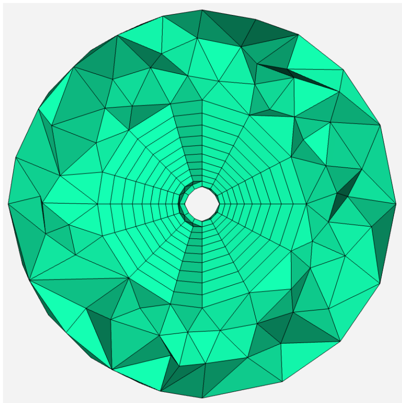

(b) Mesh around the droplet

FIGURE 8 – Geometry and mesh used during the simulation in unsteady state

5.2 Results

By introducing the following dimensionless parameters,$F' = \dfrac{F}{6\pi R_p \mu_f U_0}$ and $R' = \dfrac{R_p}{\delta} = R_p \sqrt{\dfrac{\omega}{2\nu_f}}$ that can be seen as dimensionless frequency $f' = \dfrac{f}{\left(\dfrac{\nu_f}{\pi R_p^2}\right)}$, it is possible to rewrite the equation (23) as :

$$F' = (1 + R')sin(\omega t) + R'(1 + \frac{2}{9}R')cos(\omega t) \qquad \text{with} \overrightarrow{V_p} = U_0 sin(\omega t) \tag{25}$$

The equation (25) allows us to express the variation of the dimensionless force in relation to a dimensionless radius represented in the figure 9. If the simulation takes place with a frequency of $200Hz$ and a displacement magnitude of $5.10^{-7}m$, in order to stay very small compared to the size of the droplet, we obtain the evolution of the dimensionless force experienced by the droplet over time in figure 10. This figure shows the influence of the time step on the magnitude of the force. We can see that, when the time step is reduced, the magnitude of the force acting on the surface of the droplet converge to a certain limit.

This limit is plotted in the figure 11 which represents the influence of the fluid mesh on the force acting on the surface of the droplet. The different points that can be seen in figure 12 have been calculated with a viscosity of $\mu_f = 1,856.10^{-4} Pa.s$, in order to have a low Reynolds number without having a very-low Mach number, and with

DOI: 10.13009/EUCASS2023-468

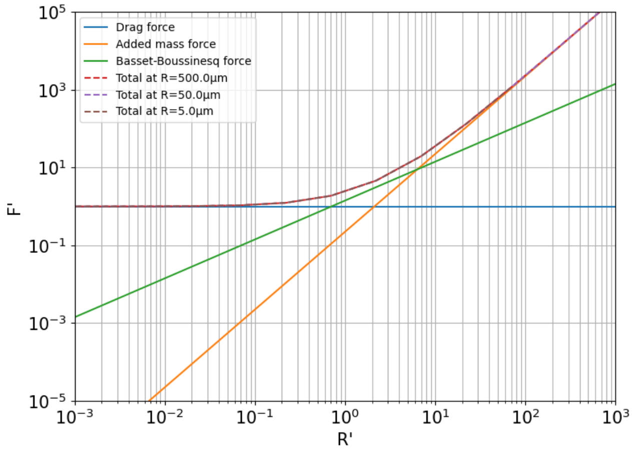

FIGURE 9 – Force acting on a droplet with dimensionless parameter

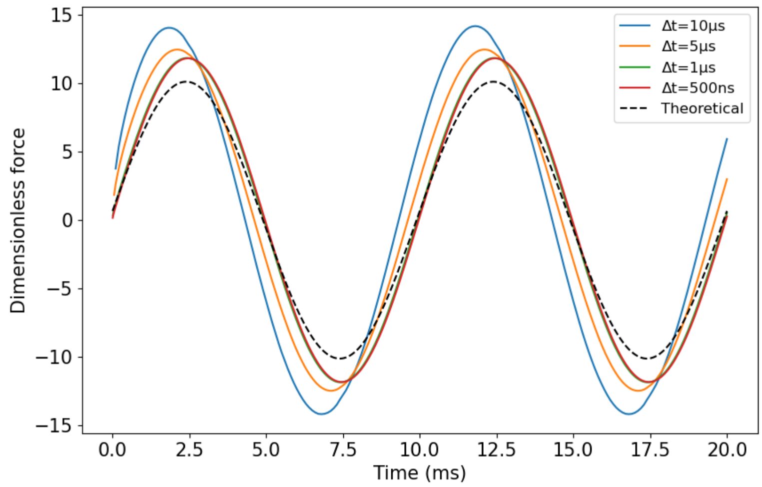

FIGURE 10 – Evolution of the dimensionless force over time for various time steps

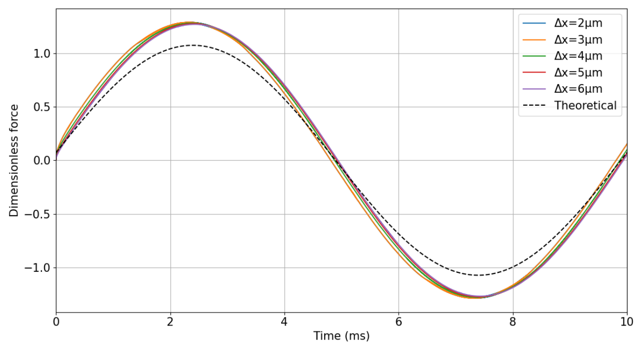

FIGURE 11 – Evolution of the dimensionless force over time for various mesh sizes

a frequency from $100Hz$ ($R' = 0,070$ and $Re = 1,97.10^{-4}$) to $1MHz$ ($R' = 7,01$ and $Re = 1,97$). As we can see in the figure 12 the numerical dimensionless force acting on the droplet follows the behavior of the resultant force calculated by Dodemand and by the BBO equation. Figure 12 shows that our numerical results are a little higher than those predicted by the equation (25).

For those simulations, the parameter that changes between our different results is the frequency of the droplet's oscillations. Even if those simulations have been made at a viscosity of $\mu_f 1,856.10^{-4} Pa.s$, the study in steady condition

DOI: 10.13009/EUCASS2023-468

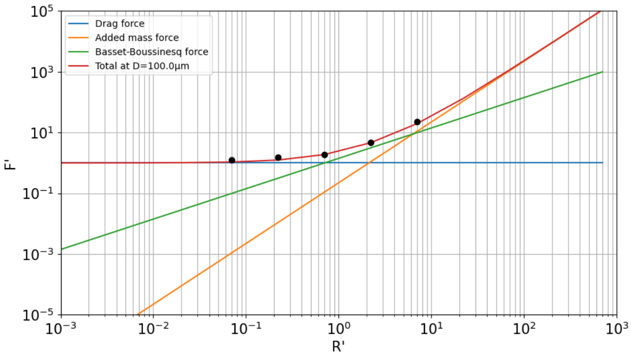

FIGURE 12 – Comparison between the theoretical and numerical force acting on the droplet

and the figure 5 shows us that the fact that is we change the viscosity or the velocity we obtain the same result. Our goal is to simulate a water droplet with air, and in order to do that, we need to see if changing the viscosity of the simulation really change the result obtained with our dimensionless parameters.

6. Conclusion and outlook

After obtaining the force experienced by the droplet in a stationary flow (equation (13)) and in the case of a rigid droplet oscillating in a fluid at rest (equation (23)), a new overlapping mesh method was introduced to obtain the force and deduce the displacement of the rigid particle. The comparison between the results obtained numerically and those obtained analytically validates the performance of the MCC in the Stokes regime as well as in the laminar regime. The introduction of rigid particle oscillation does not, a priori, affect this validation. Once we have better characterised the performance of the MCC at different Reynolds and within the limits of validity of the analytical formulae, they will be a very useful tool for simulating non-linear acoustics and developing a momentum exchange model for a single droplet. They can also be used to study heat and mass exchange between the droplet and the acoustic wave.

7. Acknowledgement

The present work was conducted thanks to a Ph.D. grant supported by Cnes (A.DYANI, technical advisor) and Onera.

Références

[1] Tim R. AUTON, J.C.R HUNT, and PRUD'HOMME. The force exerted on a body in inviscid unsteady non-uniform rotational flow. *journal of fluid mechanics*, 197 :241–257, 1988.

[2] Alfred Barnard BASSET. On the motion of a sphere in a viscous liquid. *philosophical transaction of the Royal Society of London*, page 179, Janvier 1888.

[3] Olivier BOISNEAUX. *Étude du comportement de gouttes dans un champ acoustique intense. Applications aux instabilités de combustion HF dans les moteurs-fusées*. PhD thesis, école nationale supérieure de l'aéronautique et de l'espace, 2003.

[4] Joseph BOUSSINESQ. Sur la résistance qu'oppose un liquide indéfinie en repos, sans pesanteur, au mouvement varié d'une sphère solide qu'il mouille sur toute sa surface, quand les vitesse restent bien continues et assez faibles pour que leurs carrés et produits soient négligeables. *comptes-rendus de l'Académie des sciences de Paris*, pages 935–937, Janvier-Juin 1885. tome centième.

[5] Pierre BRENNER. Three-dimensional aerodynamics with moving bodies applied to solid propellant. In *27th Joint Propulsion Conference*. American Institute of Aeronautics and Astronautics, June 1991.

[6] Amine CHADIL, Stéphane VONCENT, and Jean-Luc ESTIVALÈZES. Improvement of the viscous penalty method for particle-resolved simulations. *open journal of fluid dynamics*, 9 :168–192, 2019.

[7] Roland CLIFT, John R GRACE, and Martin E WEBER. *Bubbles, Drops and Particles*. Academic Press, 1978.

[8] F. CULICK. Combustion instabilities in solid propellant rocket motors. page 179, 01 2004.

DOI: 10.13009/EUCASS2023-468

[9] Jean-Baptiste Dargaud. *Simulation numérique de l'onde de souffle et du bruit de jet au décollage d'un lanceur*. PhD thesis, université Pierre et Marie CURIE - Paris VI, 2013.

[10] Eric Dodemand. *Comportement d'une suspension en présence d'ondes acoustiques et de tourbillons*. PhD thesis, université de Valencienne, 1994.

[11] Stany Gallier and Franck Godfroy. Aluminum combustion driven instabilities in solid rocket motors. *journal of propulsion and power*, pages 509–521, 2009.

[12] Renée Gatignol. The faxén formulae for a rigid particle in an unsteady non-uniform stokes flow. *journal de mécanique théorique et appliquée*, 2(2) :143–160, 1983.

[13] Howard H. Hu, Neelesh A. Patankar, and M.Y. Zhu. Direct numerical simulations of fluid–solid systems using the arbitrary lagrangian–eulerian technique. *journal of computational physics*, 169(2) :427–462, 2001.

[14] Max Kandula. Prediction of turbulent jet mixing noise reduction by water injection. *AIAA journal*, 46(11) :2714–2722, 2008.

[15] Ashwani K. Kapila, Ralph Menikoff, John B. Bdzil, Steven F. Son, and D. S. Stewart. Two-phase modeling of deflagration-to-detonation transition in granular materials : Reduced equations. *physics of fluids*, 13(10) :3002–3024, 10 2001.

[16] Adrien Langenais. *Adaptation des méthodes et outils aéroacoustiques pour les jets en interaction dans le cadre des lanceurs spatiaux*. PhD thesis, école centrale de Lyon, 2019.

[17] Bertrand Maury. Direct simulations of 2d fluid-particle flows in biperiodic domains. *journal of computational physics*, 156(2) :325–351, 1999.

[18] Martin R Maxey and James J Riley. Equation of motion for a small rigid sphere in a nonuniform flow. *physics of fluids*, pages 883–889, April 1983.

[19] Fuat Odar and Wallis S Hamilton. Forces on a sphere accelerating in a viscous fluid. *journal of fluid mecanics*, pages 302–314, 1964.

[20] C.W. Oseen. *Hydrodynamik*. Mathematik in Monographien und Lehrbüchern. akademische verlagsgesellschaft, 1927.

[21] Manoj Parmar, Andreas Haselbacher, and Sivaramakrishnan Balachandar. Equation of motion for a sphere in non-uniform compressible flows. *journal of fluis mechanics*, 699 :352–375, 2012.

[22] Rubén Picó, Iván Herrero-Durá, Víctor Sánchez-Morcillo, Luis J. Salmerón Contreras, and Lluís M. García-Raffi. Acoustic behavior of the vega launch pad environment, 06 2016.

[23] Georges Gabriel Stokes. On the effect of the motion internal friction of fluids on the motion of pendulums. *transactions of the Cambridge philosophical society*, page 8, Décembre 1850.

[24] Sudheer Tenneti, Rahul Garg, and Shankar Subramaniam. Drag law for monodisperse gas-solid systems using particle-resolved direct numerical simulation of flow past fiwed assemblies of spheres. *international journal of multiphase flow*, 37(9) :1072–1092, 2011.

[25] Gretar Tryggvason, Ruben Scardovelli, and Stéphane Zaleski. *Direct Numerical Simulations of Gas-Liquid Multiphase Flow*. Cambridge university press, 10 2011.